



# Oxygen vacancy engineering on copper-manganese spinel surface for enhancing toluene catalytic combustion: A comparative study of acid treatment and alkali treatment

Yu Yang<sup>a</sup>, Wenzhe Si<sup>a</sup>, Yue Peng<sup>a</sup>, Jianjun Chen<sup>a</sup>, Yu Wang<sup>b</sup>, Deli Chen<sup>a</sup>, Zhenbang Tian<sup>c</sup>, Jing Wang<sup>c</sup>, Junhua Li<sup>a,\*</sup>

<sup>a</sup> State Key Joint Laboratory of Environment Simulation and Pollution Control, School of Environment, Tsinghua University, Beijing 100084, China

<sup>b</sup> School of Environmental Science and Engineering, Yancheng Institute of Technology, Yancheng 224051, China

<sup>c</sup> Institute of Chemistry, Henan Academy of Sciences, Zhengzhou 450003, China

## ARTICLE INFO

### Keywords:

Copper-manganese spinel  
Catalytic combustion  
Toluene  
Oxygen vacancy engineering  
Selective dissolution

## ABSTRACT

Copper-manganese spinel is a low-cost VOCs catalytic combustion catalyst with good performance. Oxygen vacancy has excellent properties for oxygen activation and VOCs dehydrogenation activation, which is beneficial for the catalytic combustion of VOCs. In this study, a large number of oxygen vacancies were introduced on the copper-manganese spinel surface by selective dissolution method (acid treatment and alkali treatment) for catalytic combustion of toluene. Furthermore, the effects of acid treatment and alkali treatment on the catalytic performance, oxygen vacancy amount, physical and chemical properties, and toluene catalytic combustion mechanism of copper-manganese spinel were studied. Both acid treatment and alkali treatment can produce large quantities of oxygen vacancies on the copper-manganese spinel surface. The generation of surface oxygen vacancies can greatly improve the catalytic combustion activity of copper-manganese spinel. At 240 °C, the combustion rate of toluene increased by 8.8 times for the acid-treated catalyst and 11.2 times for the alkali-treated catalyst. The numerous surface oxygen vacancies,  $\text{Mn}^{3+}/\text{Mn}^{4+}$  at the ratio of 1.11 and appropriate acidity result in the alkali-treated catalyst exhibiting excellent catalytic activity and stability for toluene combustion. This strategy provides a new method to further improve catalytic combustion activity of copper-manganese spinel and a reference for the development of the surface oxygen vacancy engineering of transition metal oxides.

## 1. Introduction

The elimination of volatile organic compounds (VOCs) is one of the important tasks of environmental protection in the world [1,2]. VOCs not only cause direct harm to human health, but also are the essential precursors to haze and ozone [3–5]. Catalytic combustion is considered to be one of the most promising VOCs removal technologies due to its economical and effective characteristics [6–8]. The supported noble metal catalysts are commonly used in the field of catalytic combustion [9,10]. In recent decades, noble metal catalysts have been widely used in industrial catalysis, resulting in substantial annual consumption of noble metals. However, noble metal reserves are scarce. In contrast, earth-abundant metals (EAMs) have a vast amount of reserves,  $10^4$  times that of noble metals [11]. Therefore, EAMs are much cheaper than noble

metals. The copper-manganese spinel is a typical EAMs oxide with good performance in environmental catalysis field [12–15]. In the application of VOCs catalytic combustion, copper-manganese spinel not only has good catalytic activity, but also has excellent catalytic stability, which makes copper-manganese spinel a promising substitute for noble metal catalyst [16].

It is reported that oxygen vacancies contribute to the catalytic combustion of VOCs. Liu et al. found that oxygen vacancy had a strong ability to adsorb and dissociate oxygen. In addition, increasing the amount of oxygen vacancies of the catalyst can significantly improve the catalytic combustion activity of VOCs [17]. Friedrich et al. reported that oxygen vacancy could also enhance the dehydrogenation activation of VOCs, which greatly accelerated the catalytic oxidation rate of VOCs [18]. Oxygen vacancy engineering is an efficient method to improve the

\* Corresponding author.

E-mail address: [lijunhua@tsinghua.edu.cn](mailto:lijunhua@tsinghua.edu.cn) (J. Li).

<https://doi.org/10.1016/j.apcatb.2023.123142>

Received 17 May 2023; Received in revised form 11 July 2023; Accepted 31 July 2023

Available online 1 August 2023

0926-3373/© 2023 Elsevier B.V. All rights reserved.

catalytic activity of transition metal oxides, which is widely used in photocatalysis, electrocatalysis, thermal catalysis, especially catalytic combustion [19–22]. Attempts have been made to improve the catalytic combustion activity of manganese-based catalysts by oxygen vacancy engineering. Fu et al. increased the number of oxygen vacancies by doping cerium into the manganese oxides, and Shi et al. found that doping cobalt into manganese oxides could introduce many oxygen vacancies [23,24]. Although the metal doping method can increase the amount of oxygen vacancies, many oxygen vacancies exist in the bulk phase of the catalyst. The catalytic combustion of VOCs only occurs on catalyst's surface, and the oxygen vacancy in the bulk phase does not participate in the catalytic reaction [25,26]. It is reported that the selective dissolution of A-site metals in an acidic solution can introduce oxygen vacancies on the surface of perovskite-type catalysts [27–29]. To our best knowledge, few studies were reported on the oxygen vacancy engineering of introducing oxygen vacancies on the surface of spinel catalysts by selective dissolution method.

Herein, we successfully introduced numerous oxygen vacancies on the copper-manganese spinel surface through the selective dissolution method (acid treatment and alkali treatment). The selective dissolution method can dissolve the  $\text{Cu}^{2+}$  oxides on the surface of copper-manganese spinel, and the removal of  $\text{Cu}^{2+}$  oxides can introduce a large number of oxygen vacancies on the surface of copper-manganese spinel. Both acid treatment and alkali treatment could significantly improve the catalytic activity of copper-manganese spinel for toluene combustion. In addition, the effects of acid and alkali treatment on the oxygen vacancy amount, physicochemical properties, toluene catalytic combustion mechanism, and catalytic stability of copper-manganese spinel were investigated to compare the characteristics of two selective dissolution methods. The catalytic combustion activity of an alkali-treated catalyst is higher than that of an acid-treated catalyst since an alkali-treated catalyst has more oxygen vacancies and an appropriate  $\text{Mn}^{3+}/\text{Mn}^{4+}$  mole ratio. Only  $\text{Mn}_2\text{O}_3$  crystals were formed on the alkali-treated catalyst surface, which preserved oxygen vacancies to the maximum extent. In situ NAP-XPS results showed that oxygen vacancies can activate oxygen and enhance adsorbed oxygen's oxidation capacity on the surface. The appropriate acidity of the catalyst render the alkali-treated catalyst with excellent catalytic stability for toluene combustion. Our findings provide a new technique to enhance the catalytic combustion activity of copper-manganese spinel and also supply a low-cost and high-efficiency method for the surface oxygen vacancy engineering development of transition metal oxides, which may has huge potential in other catalysis fields.

## 2. Experimental

### 2.1. Catalyst preparation

Adding appropriate amount of ammonia to the mixed solution of copper nitrate ( $\text{Cu}(\text{NO}_3)_2 \cdot 3\text{H}_2\text{O}$ ), manganese nitrate ( $\text{Mn}(\text{NO}_3)_2$ , 50 wt % in water) and citric acid ( $\text{C}_6\text{H}_8\text{O}_7$ ) to adjust the pH to 9.3. Then, the wet gel obtained through continuously stirring the mixed solution under 90 °C water bath. The wet gel was treated at 200 °C in air for 3 h, and then calcinated at 400 °C for 3 h, the obtained copper-manganese spinel catalyst named CMO.

**Acid treatment:** Using 3 M nitric acid solution to treat the CMO for 15, 30, 45, 60, and 90 min, respectively. After that, filtering and washing the samples with deionized water. Then, the samples dried at 100 °C in air. The obtained catalysts named CMO-AC15, CMO-AC30, CMO-AC45, CMO-AC60 and CMO-AC90, respectively.

**Alkali treatment:** The CMO was treated by 3 M sodium hydroxide solution for 30, 45, 60, 75 and 90 min, respectively. Then, filtering and washing the samples with deionized water. After that, the samples dried at 100 °C in air. The obtained catalysts named CMO-ALK30, CMO-ALK45, CMO-ALK60, CMO-ALK75 and CMO-ALK90, respectively.

### 2.2. Characterization

The X-ray diffraction (XRD) studies were performed on Bruker D8 Advance. The electron microscopy images (HR-TEM) were obtained on JEM-2010 F. The  $\text{N}_2$  adsorption-desorption was performed on Quantachrome Autosorb-1MP. The electron paramagnetic resonance (EPR) detections were gained on Bruker A300–10. The X-ray photoelectron spectroscopy (XPS) was carried out on Thermo Fisher K-Alpha. The in situ NAP-XPS experiments were conducted on the SPECS instrument. The temperature-programmed reduction of hydrogen ( $\text{H}_2$ -TPR) was performed on Micromeritics Chemisorb 2920. The temperature-programmed desorption of ammonia ( $\text{NH}_3$ -TPD) was performed on Auto Chem II 2920. The oxygen temperature-programmed desorption ( $\text{O}_2$ -TPD) were obtained on Micromeritics Chemisorb 2920. The in situ diffuse reflectance infrared Fourier transform spectroscopy (In situ DRIFT) was carried out on Thermo Fisher NICOLET6700 FTIR. The details of characterizations are listed in [Supporting Information](#).

### 2.3. Catalytic evaluation

In a fixed-bed microreactor, the catalytic activity and stability of the catalysts (0.1 g, 40–60 mesh) were tested. The details are listed in [Supporting Information](#).

The toluene or CO conversion ( $X_{\text{toluene or CO}}$ , %) is calculated by the following equation:

$$X_{\text{toluene or CO}}(\%) = 100 \times \frac{[\text{toluene or CO}]_{\text{in}} - [\text{toluene or CO}]_{\text{out}}}{[\text{toluene or CO}]_{\text{in}}}$$

The  $[\text{toluene or CO}]_{\text{in}}$  and  $[\text{toluene or CO}]_{\text{out}}$  are the inlet and outlet concentrations of toluene or CO, respectively.

The surface area normalized reaction rate ( $r$ ,  $\text{mol} \cdot \text{m}^{-2} \cdot \text{s}^{-1}$ ) is calculated by the following equation:

$$r(\text{mol} \cdot \text{m}^{-2} \cdot \text{s}^{-1}) = - \frac{C_{\text{inlet}} \cdot F}{m_{\text{cat}} \cdot S_{\text{BET}}} \cdot \ln(1 - X_{\text{toluene or CO}})$$

The  $C_{\text{inlet}}$  is the toluene or CO concentration in the inlet gas, the flow rate is represented by  $F$  (mol/s),  $m_{\text{cat}}$  (g) is the mass of the catalyst, and the surface area of the catalyst is  $S_{\text{BET}}$  ( $\text{m}^2/\text{g}$ ).

## 3. Results and discussion

### 3.1. Catalytic activity of toluene combustion

The effect of treatment times on the catalytic activity of  $\text{CuMn}_2\text{O}_4$  spinel for toluene combustion were studied, and the results are shown in Fig. 1(a, b). The results show that both acid treatment and alkali treatment can improve the catalytic combustion activity of  $\text{CuMn}_2\text{O}_4$  spinel, and the treatment time has a great influence on the catalytic activity. With the increase of acid and alkali treatment time, the catalytic combustion activity first increased and then decreased slightly. The optimal time for acid treatment and alkali treatment is 45 min and 60 min, respectively. For convenience, the catalytic activities of the optimal catalysts were compared by conversion rate and surface area normalized reaction rate, and the results are shown in Fig. 1(c, d). The results showed that both acid treatment and alkali treatment greatly increased the catalytic activity of  $\text{CuMn}_2\text{O}_4$  spinel for toluene combustion. The catalytic performance of CMO-AC45 and CMO-ALK60 are almost the same in conversion rate, but the surface area normalized reaction rate of CMO-ALK60 is much higher than that of CMO-AC45. The surface area normalized reaction rates at 240, 250, and 260 °C are expressed as  $r_{240}$ ,  $r_{250}$ , and  $r_{260}$ , respectively. The  $r_{240}$  of CMO, CMO-AC45 and CMO-ALK60 are  $1.56 \times 10^{-9}$ ,  $1.38 \times 10^{-8}$  and  $1.75 \times 10^{-8} \text{ mol} \cdot \text{m}^{-2} \cdot \text{s}^{-1}$ , respectively, the  $r_{250}$  are  $4.05 \times 10^{-9}$ ,  $3.11 \times 10^{-8}$  and  $4.72 \times 10^{-8} \text{ mol} \cdot \text{m}^{-2} \cdot \text{s}^{-1}$ , and the  $r_{260}$  are  $1.65 \times 10^{-8}$ ,  $4.39 \times 10^{-8}$  and  $7.05 \times 10^{-8} \text{ mol} \cdot \text{m}^{-2} \cdot \text{s}^{-1}$  respectively. The results indicate that the catalytic combustion activity of the catalysts increases in the order: CMO < CMO-

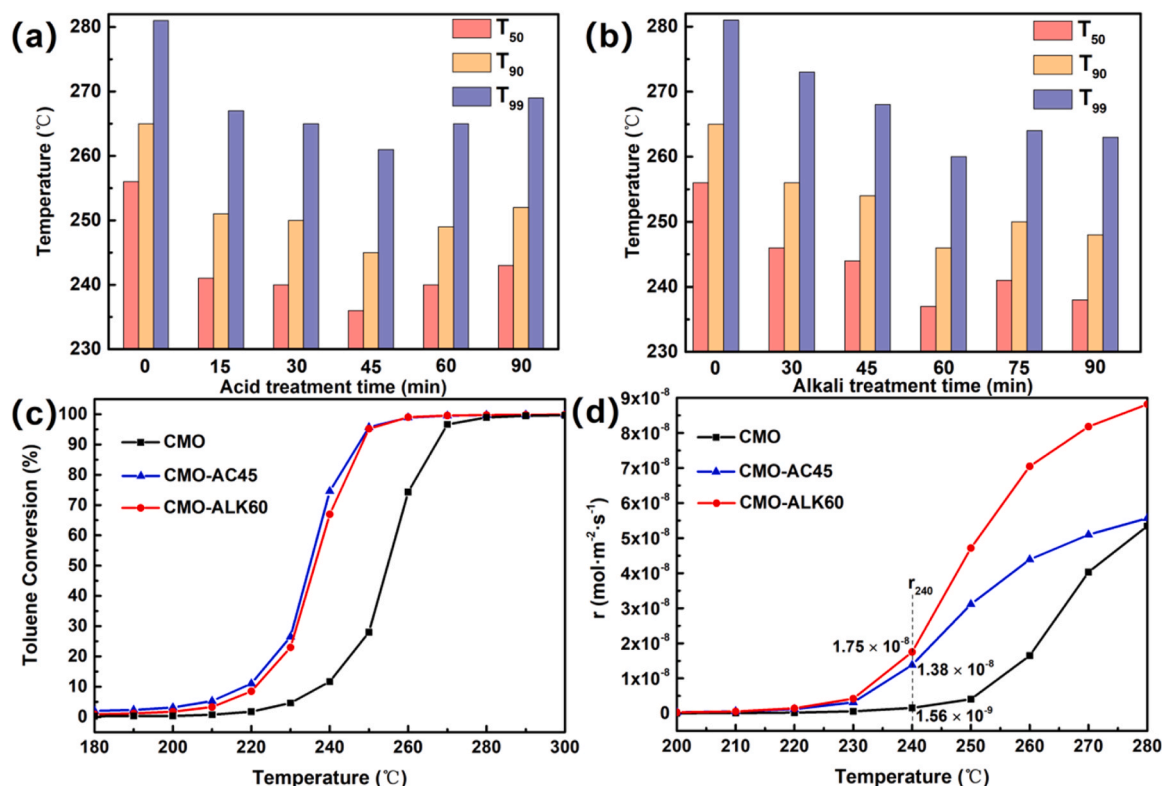


Fig. 1. Catalytic combustion performance of toluene on the catalysts with different (a) acid-treated and (b) alkali-treated time. (c) Toluene Conversion of CMO, CMO-AC45 and CMO-ALK60. (d) Surface area normalized reaction rates of CMO, CMO-AC45 and CMO-ALK60.

AC45 < CMO-ALK60.

Fig. S1 shows the CO<sub>2</sub> yield at different temperatures, and the results indicate that the CO<sub>2</sub> yield follows the same order in terms of conversion rate (Fig. 1c). In addition, the CO concentrations of outlet gas at different reaction temperatures were detected, and the results are shown in Fig. S2. The results show that the temperatures at the highest CO concentration of CMO-AC45 and CMO-ALK60 are lower than that of CMO. Furthermore, the CO concentration of CMO-ALK60 is lower than that of CMO-AC45 before 245 °C, and the CO concentrations of the two catalysts are basically the same after 245 °C and gradually decrease to 0 ppm. To further explain this phenomenon, the CO catalytic oxidation activity of the catalysts was detected, and the results are shown in Figs. S3 and S4. Both acid treatment and alkali treatment promoted the catalytic oxidation activity of CuMn<sub>2</sub>O<sub>4</sub> spinel for CO, and the catalytic activity of the catalysts increased in the following order: CMO < CMO-AC45 < CMO-ALK60 (conversion rate and surface area normalized reaction rate). According to reports, CO mainly reacts with the surface adsorbed oxygen (O<sub>ads</sub>) on the spinel and perovskite oxides with rich oxygen vacancies [30,31]. The O<sub>2</sub>-TPD is used to detect the mobility of lattice oxygen (O<sub>latt</sub>) of the catalysts, and the results are shown in Fig. S5. The O<sub>latt</sub> mobility of CMO-AC45 is lower than that of CMO, and the CO oxidation activity of CMO-AC45 is higher than that of CMO, which further proves that CO mainly reacts with O<sub>ads</sub> on the spinel oxides with rich oxygen vacancies. The CO oxidation activity can reflect that the introduction of surface oxygen vacancies can enhance the ability of the catalyst to adsorb and activate oxygen. In addition, it has been reported that both O<sub>ads</sub> and O<sub>latt</sub> on the spinel catalyst with rich oxygen vacancies can effectively oxidize toluene [32]. The CMO-AC45 and CMO-ALK60 can provide more active surface adsorbed oxygen for toluene oxidation.

### 3.2. Structural and chemical characterization

The effects of acid treatment and alkali treatment on the crystal

structure of CuMn<sub>2</sub>O<sub>4</sub> spinel were studied by XRD, and the results are shown in Fig. 2. The structure of CMO catalyst belongs to JCPDS 74-2422 (CuMn<sub>2</sub>O<sub>4</sub> spinel). The Mn<sub>2</sub>O<sub>3</sub> crystals were formed on the surface of CuMn<sub>2</sub>O<sub>4</sub> spinel by both acid treatment and alkali treatment. Only Mn<sub>2</sub>O<sub>3</sub> (222) crystal was formed on the surface of alkali-treated catalysts. In contrast, Mn<sub>2</sub>O<sub>3</sub> (211), Mn<sub>2</sub>O<sub>3</sub> (222), Mn<sub>2</sub>O<sub>3</sub> (400), Mn<sub>2</sub>O<sub>3</sub> (332), and Mn<sub>2</sub>O<sub>3</sub> (440) were formed on the surface of acid-treated catalysts. It reveals that acid treatment is more likely to dissolve Cu species on the CuMn<sub>2</sub>O<sub>4</sub> spinel surface than alkali treatment, and more Cu species are removed by acid treatment, resulting in more Mn<sub>2</sub>O<sub>3</sub> species on the surface of the acid-treated catalyst. After acid and alkali treatment, the catalysts still have diffraction peaks of CuMn<sub>2</sub>O<sub>4</sub> spinel (111, 220, 311, 400, 331, 422, 511, 400, 531 and 622), indicating that the acid and alkali treatment only selectively dissolved the metal oxides on the catalyst surface without affecting the bulk phase of the catalysts. For further studying the dissolution of metal oxides by acid and alkali treatment, the ICP tests were performed on the post-reaction acid and alkali solutions, and the ICP results are shown in Table 1. The post-reaction acid solution contains 421.6 µg/L Cu ion and 231.1 µg/L Mn ion, and the content of Cu ion is almost twice that of Mn ion, revealing that acid treatment can dissolve both Cu species and Mn species on the surface of CuMn<sub>2</sub>O<sub>4</sub> spinel. By contrast, the post-reaction alkali solution contains 170.3 µg/L Cu ion and 6.7 µg/L Mn ion, confirming that alkali treatment can only dissolve Cu species on the surface of CuMn<sub>2</sub>O<sub>4</sub> spinel and hardly dissolve Mn species. Furthermore, the content of Cu ion in the post-reaction acid solution is about 2.5 times that in the post-reaction alkali solution, which demonstrates that the Cu species on the surface of CuMn<sub>2</sub>O<sub>4</sub> spinel can be dissolved more easily by acid treatment. And the ICP results is consistent with the XRD results.

Fig. 3 and Table 2 show the results of the N<sub>2</sub> adsorption-desorption experiment. The adsorption-desorption isotherms of the catalysts, shown in Fig. 3a, are all H3-type, which proves that all catalysts are typical mesoporous materials [33]. Fig. 3b and c show the pore size distribution of the catalysts. Acid treatment can dissolve both Cu and Mn

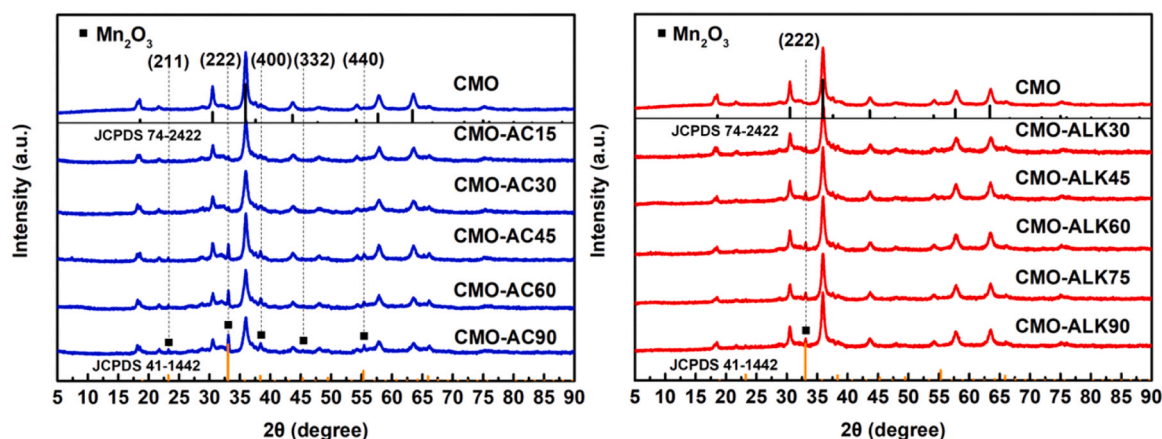


Fig. 2. XRD patterns of the catalysts.

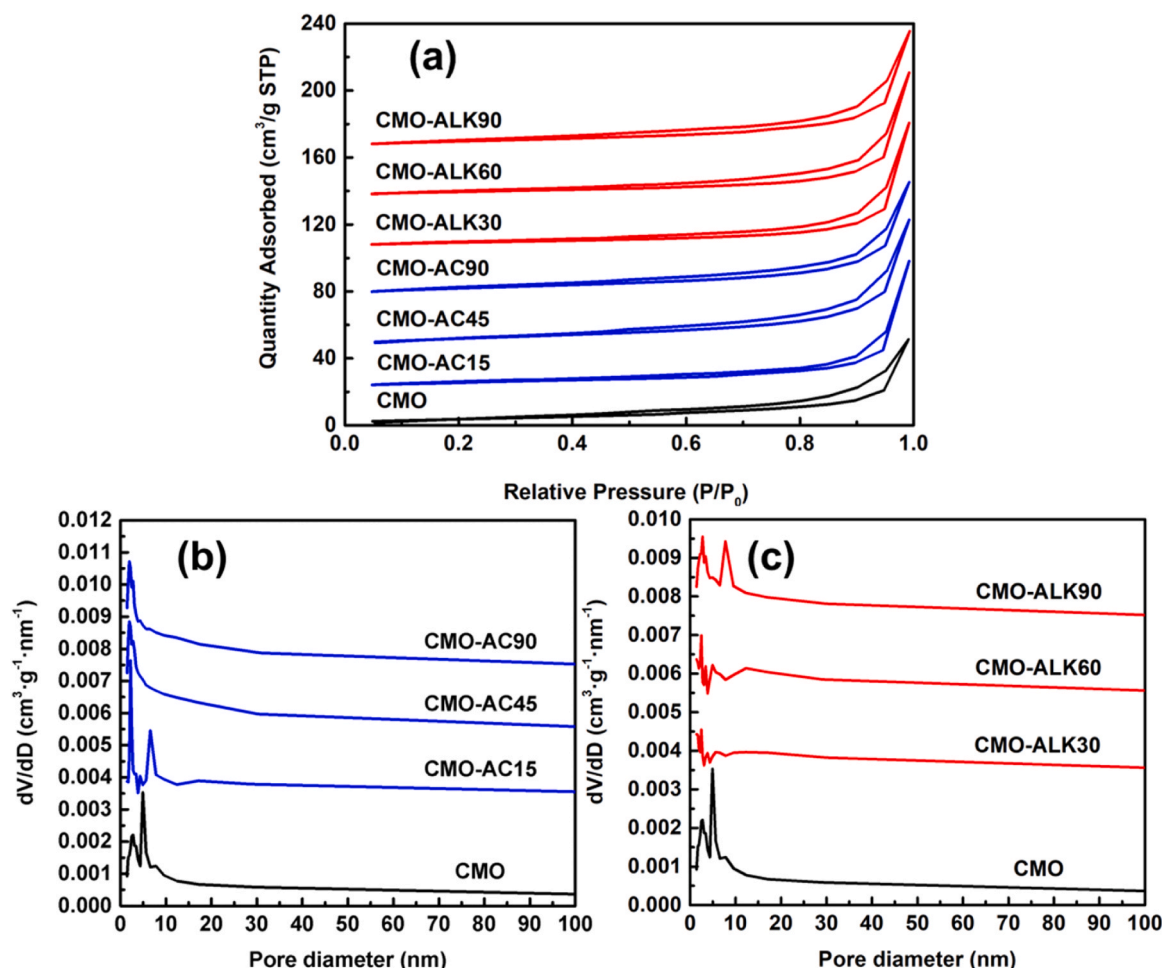
Table 1

ICP results of the catalysts.

Catalyst	Cu content in solution (ug/L)	Mn content in solution (ug/L)	Cu content in catalyst (wt%)	Mn content in catalyst (wt%)
CMO-AC45	421.6	231.1	22.90	40.32
CMO-ALK60	170.3	6.7	23.22	40.81

species, resulting in dissolution and perforation of the pore wall during acid treatment, which increases the surface area and pore volume of the acid-treated catalyst [34,35]. The larger surface area can expose more catalytic active sites, which is beneficial to VOCs catalytic combustion [36,37]. In contrast, alkali treatment can only dissolve Cu species, which causes partial pores to collapse into larger pores in the process of alkali solution agitation. Thus, it increased the pore volume and reduced the surface area of alkali-treated catalysts.

The morphology and crystal state changes of the acid-treated and

Fig. 3. (a)  $N_2$  adsorption-desorption isotherms. (b, c) Pore size distribution of the catalysts.



**Table 2**

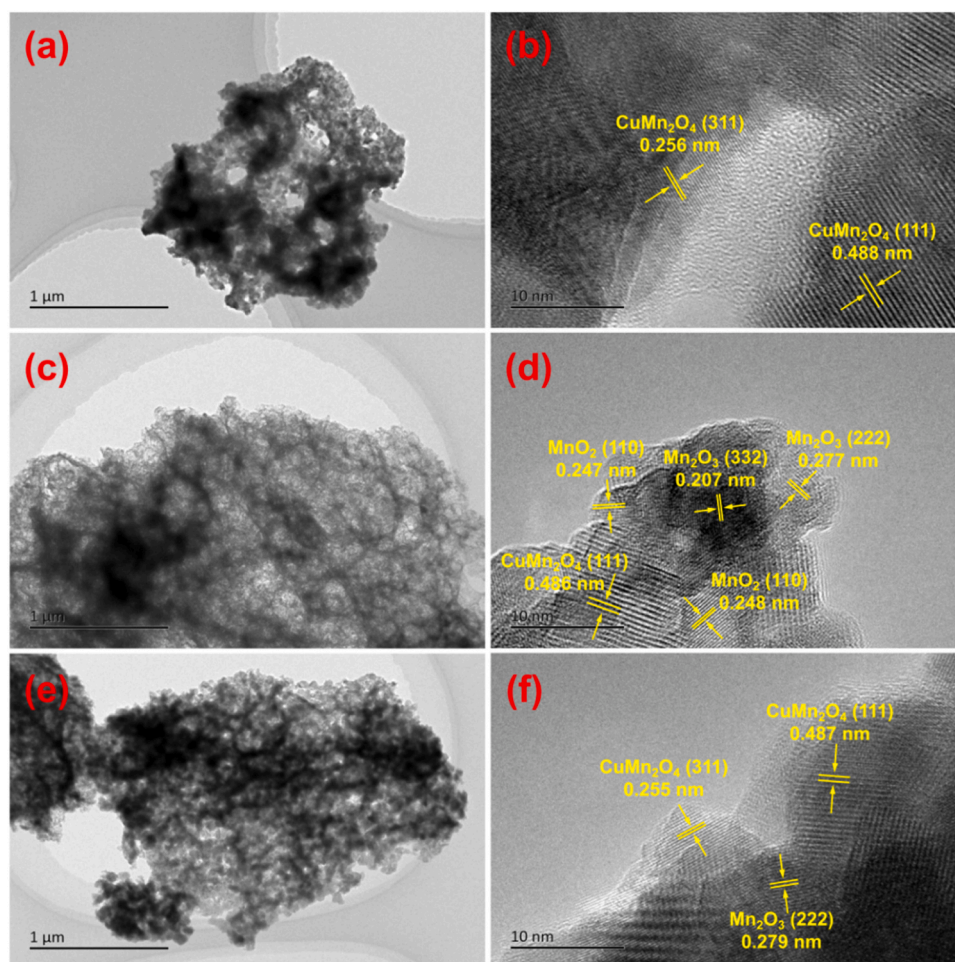
BET results and surface atomic ratios of the catalysts.

Catalyst	BET		XPS			
	Surface area ( $\text{m}^2 \text{g}^{-1}$ )	Pore volume ( $\text{cm}^3 \text{g}^{-1}$ )	Mn <sup>3+</sup> /Mn <sup>4+</sup> molar ratio	O atomic %	Mn atomic %	Cu atomic %
CMO	31.631	0.088	0.630	58.83	30.18	10.99
CMO-AC15	33.13	0.122	/	/	/	/
CMO-AC45	39.257	0.126	0.738	61.78	31.07	7.15
CMO-AC90	36.368	0.112	0.682	62.83	32.11	5.06
CMO-ALK30	22.416	0.119	/	/	/	/
CMO-ALK60	25.102	0.121	1.11	58.17	32.38	9.45
CMO-ALK90	29.857	0.114	1.30	58.07	32.92	9.01

alkali-treated catalysts were observed by HR-TEM, and the results are shown in Fig. 4. The CMO-AC45 exhibited a cotton-like structure, and the CMO-ALK60 expressed a sponge-like structure, proving that acid treatment is easier to dissolve metal oxides than alkali treatment (Fig. 4a, c, e). The cotton-like structure makes the surface area of CMO-AC45 larger than that of CMO. In addition, the surface of CMO-AC45 not only contains  $\text{Mn}_2\text{O}_3$  and  $\text{CuMn}_2\text{O}_4$  spinel crystals but also has  $\text{MnO}_2$  (110) nanocrystal particles. And the  $\text{MnO}_2$  nanocrystal particles are highly dispersed on the catalyst surface, which makes the XRD pattern of CMO-AC45 have no diffraction peak of  $\text{MnO}_2$  crystal. The nitric acid can disproportionate with  $\text{Mn}_2\text{O}_3$  to generate  $\text{MnO}_2$ , and the chemical reaction equation is:  $2\text{HNO}_3 + \text{Mn}_2\text{O}_3 \rightarrow \text{MnO}_2 + \text{Mn}(\text{NO}_3)_2 + \text{H}_2\text{O}$  [29, 33]. This reaction occurs weakly in the dilute nitric acid, resulting in highly dispersed  $\text{MnO}_2$  nanocrystal particles rather than a single large crystal [38]. Moreover, the  $\text{MnO}_2$  has excellent catalytic combustion activity, which is one of the reasons that the catalytic activity of

CMO-AC45 is higher than that of CMO [34,39]. In contrast, the surface of CMO-ALK60 has only  $\text{Mn}_2\text{O}_3$  and  $\text{CuMn}_2\text{O}_4$  spinel crystals. Since the alkali treatment can only dissolve Cu species on the surface of  $\text{CuMn}_2\text{O}_4$  spinel, only  $\text{Mn}_2\text{O}_3$  crystal was formed on the catalyst surface.

Using XPS analysis to investigate the chemical state of Mn species. The peak fitting for Mn 2p<sub>3/2</sub> peaks and the Mn<sup>3+</sup>/Mn<sup>4+</sup> ratios are shown in Fig. 5 and Table 2.  $\text{Mn}_2\text{O}_3$  was generated during the acid treatment and alkali treatment on the surface of the catalysts, which reduced the valence state of Mn species of the catalysts, which reduced the valence state of Mn species of the catalysts. Since the disproportionation reaction between nitric acid and  $\text{Mn}_2\text{O}_3$ , the Mn<sup>3+</sup>/Mn<sup>4+</sup> ratio of the acid-treated catalyst is lower than that of the alkali-treated catalyst. The results of the XPS analysis are in good agreement with the XRD and HR-TEM results. It has been reported that the catalytic combustion activity of manganese-based catalysts is the highest when the Mn<sup>3+</sup>/Mn<sup>4+</sup> ratio is about 1.1 [40]. The excellent catalytic activity for VOCs combustion is attributed to the double-exchange behavior

**Fig. 4.** HR-TEM images of the catalysts: (a, b) CMO, (c, d) CMO-AC45 and (e, f) CMO-ALK60.

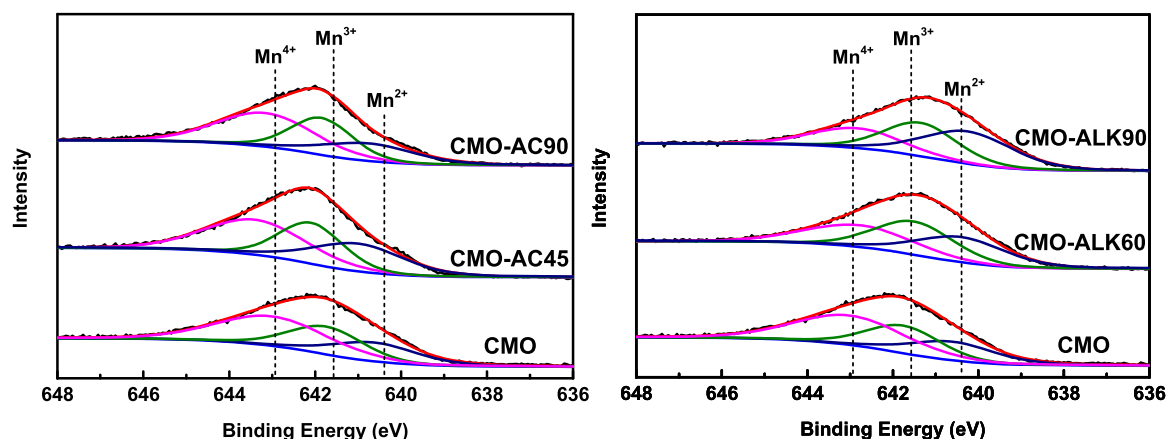


Fig. 5. Mn  $2p_{3/2}$  XPS spectra of the catalysts.

between  $Mn^{3+}$  and  $Mn^{4+}$ . Interestingly, the  $Mn^{3+}/Mn^{4+}$  ratio of CMO-ALK60 with the highest activity is 1.11, which can facilitate electron transfer between manganese-based active components. Furthermore, the percentage of surface Cu atoms decreased and the percentage of surface Mn atoms increased after acid treatment and alkali treatment, which also proved that numerous Cu species on the  $CuMn_2O_4$  spinel surface were removed by acid and alkali treatment. The selective dissolution of metal oxides could introduce a large number of oxygen vacancies on the surface of  $CuMn_2O_4$  spinel. To further observe the amount of oxygen vacancies introduced by acid and alkali treatment, the EPR test was used to detect the changes of oxygen vacancies of the catalyst.

### 3.3. Oxygen vacancies and surface active oxygen species

Fig. 6 shows the EPR results of the catalysts. The results illustrates that both acid and alkali treatment could produce oxygen vacancies on the  $CuMn_2O_4$  spinel surface, and the amount of oxygen vacancies of the catalysts increases in the following order: CMO < CMO-AC45 < CMO-ALK60. In addition, the Raman spectra is used to further detect the structure of the catalysts, and the results are presented in Fig. S6. He et al. have found that as oxygen vacancies increase in spinel oxides, the B-O peak at  $600\text{--}700\text{ cm}^{-1}$  shifts towards higher Raman shift ( $AB_2O_4$  spinel, with the metal B occupying an octahedral position) [41]. The Raman results in Fig. S6 show that the Raman shift of Mn-O peak increases in the order: CMO < CMO-AC45 < CMO-ALK60, which is consistent with the increasing order of the oxygen vacancies amount. In addition, an increase in the number of oxygen vacancies will lead to an increase in the surface disorder of spinel. Therefore, the more oxygen

vacancies on the surface, the wider the Mn-O peak at  $600\text{--}700\text{ cm}^{-1}$ . The Raman results are consistent with the EPR results, and the changes in Raman spectra may be caused by the changes in oxygen vacancies. The oxygen vacancy can accelerate the adsorption and activation of oxygen and increase the content of surface active oxygen species [21,42]. Therefore, the formation of oxygen vacancy is beneficial to improve the catalytic activity of the catalyst for VOCs combustion [22]. In contrast, the amount of oxygen vacancies on the surface of CMO-ALK60 is much higher than that of CMO-AC45. Some oxygen vacancies may be destroyed in the disproportionation reaction between nitric acid and  $Mn_2O_3$ . The alkali treatment can only selectively dissolve Cu species, leaving more oxygen vacancies on the surface of CMO-ALK60 [43,44]. The alkali treatment is superior to the acid treatment in the preparation of oxygen vacancy on  $CuMn_2O_4$  spinel surface, which is one of the reasons for the higher activity of CMO-ALK60 than CMO-AC45.

The O 1s in-situ XPS detection was carried out on the catalyst to further study the effects of acid treatment and alkali treatment on the oxygen activation and the ability of surface active oxygen species to participate in the oxidation reaction. Fig. 7(a-c) and Table 3 show the changes of adsorbed oxygen ( $O_{ads}$ ) on the catalyst with increasing temperature under oxygen pass-through condition. The  $O_{ads}$  content on the CMO and CMO-AC45 increased continuously from  $100\text{ }^{\circ}\text{C}$  to  $200\text{ }^{\circ}\text{C}$  and decreased at  $250\text{ }^{\circ}\text{C}$ , while the  $O_{ads}$  content on the CMO-ALK60 surface decreased continuously with increasing temperature. It demonstrates that the  $O_{ads}$  on CMO-ALK60 has stronger mobility. The high mobility of surface active oxygen species is conducive to the VOCs oxidation reaction. The maximum and minimum  $O_{ads}$  content on the catalyst are shown in Table 3. The adsorption capacity of the catalysts for oxygen increases in the order: CMO < CMO-ALK60 < CMO-AC45. Although the amount of oxygen vacancies on the CMO-AC45 surface is lower than that of CMO-ALK60, the surface area of CMO-AC45 ( $39.257\text{ m}^2\cdot\text{g}^{-1}$ ) is higher than that of CMO-ALK60 ( $25.102\text{ m}^2\cdot\text{g}^{-1}$ ), and the larger surface area allows CMO-AC45 to adsorb more oxygen. However, with the increase in temperature, the desorption amount of  $O_{ads}$  ( $\Delta O_{ads}(O_2)$ ) increases in the following order: CMO < CMO-AC45 < CMO-ALK60, which further confirms that the fluidity of active oxygen species on CMO-ALK60 surface is the highest. Fig. 7(d-f) and Table 3 show the changes in  $O_{ads}$  content on the catalyst with the increase in temperature under  $CO + O_2$  passing through. The  $O_{ads}$  content on the CMO and CMO-AC45 first increased and then decreased during the heating process. In contrast, the  $O_{ads}$  content on the CMO-ALK60 decreased continuously with the increase in temperature. In addition, Table 3 shows the maximum and minimum  $O_{ads}$  content on the catalyst. The results show that the surface active oxygen species on CMO-ALK60 is the most likely to react with CO, and the oxidation capacity of surface active oxygen species ( $\Delta O_{ads}(CO+O_2)$ ) increases in the order: CMO < CMO-AC45 < CMO-ALK60. The above O 1s in-situ XPS results show

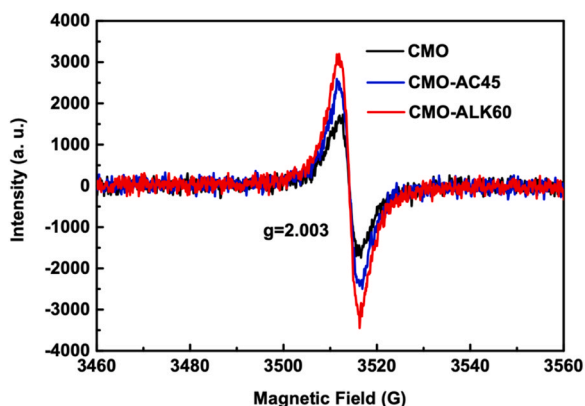
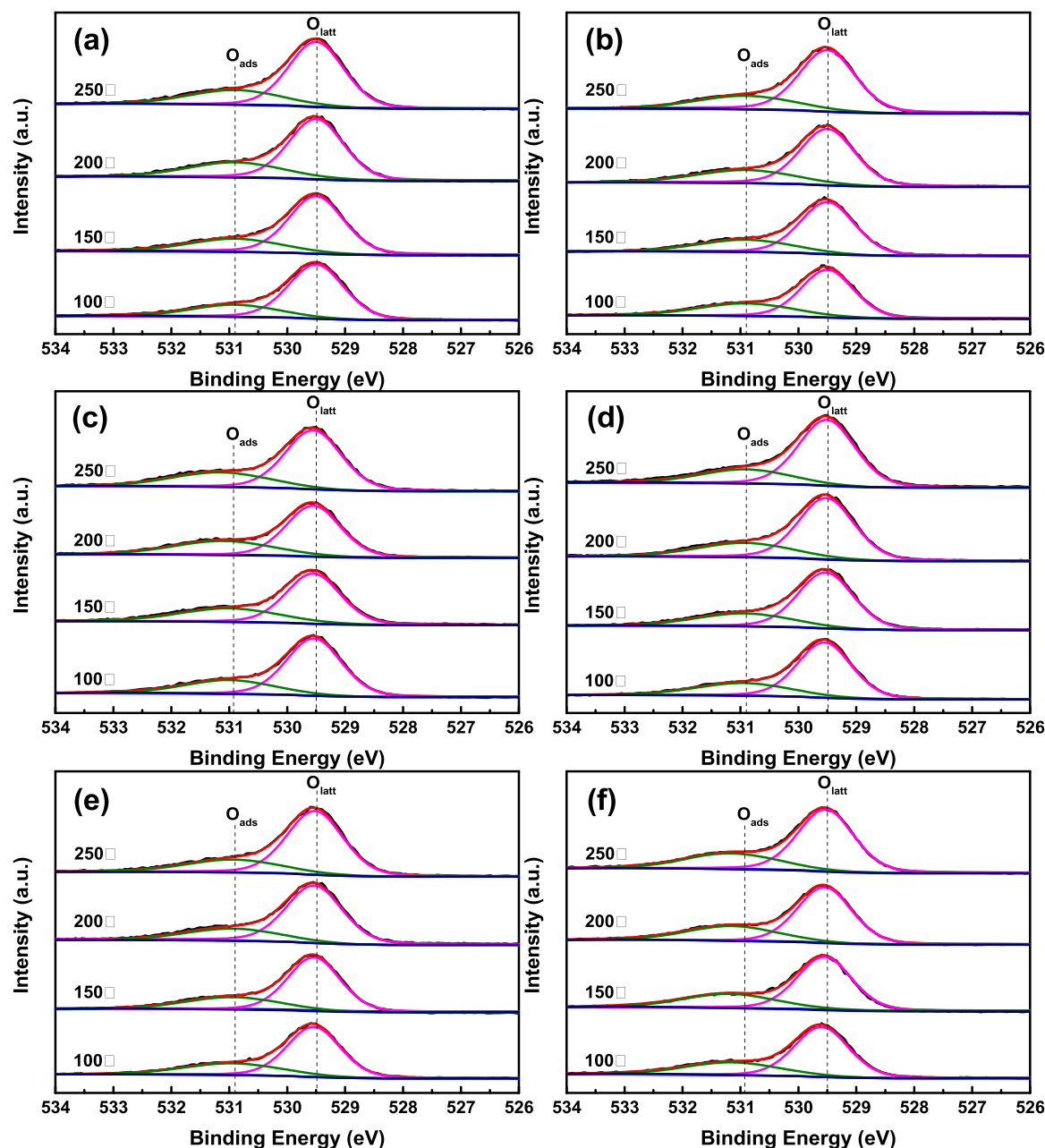


Fig. 6. EPR spectra of the catalysts. The data for CMO and CMO-ALK60 are referenced from our previous work.[31].



**Fig. 7.** In situ NAP-XPS of O 1s (a-c) oxygen pass through: (a) CMO, (b) CMO-ALK60, (c) CMO-AC45; (d-f) CO + O<sub>2</sub> pass through (CO:O<sub>2</sub> = 1:1): (d) CMO, (e) CMO-ALK60, (f) CMO-AC45. The total pressure in the NAP cell was fixed to 2 mbar for CMO, CMO-ALK60 and CMO-AC45. The data for CMO and CMO-ALK60 are referenced from our previous work.[31].

**Table 3**

In situ NAP-XPS of O 1s ( $\Delta O_{\text{ads}} = \text{maximum } O_{\text{ads}}/O_{\text{altt}} - \text{minimum } O_{\text{ads}}/O_{\text{altt}}$ ).

Catalyst-temperature	$O_{\text{ads}}/O_{\text{altt}}$ (O <sub>2</sub> )	$O_{\text{ads}}/O_{\text{altt}}$ (CO+O <sub>2</sub> )	$\Delta O_{\text{ads}}$ (O <sub>2</sub> )	$\Delta O_{\text{ads}}$ (CO+O <sub>2</sub> )
CMO-100	0.3494	0.4076		
CMO-150	0.3945	0.4285		
CMO-200	0.4265	0.4172		
CMO-250	0.3914	0.3846	0.0351	0.0439
CMO-ALK60-100	0.4803	0.4289		
CMO-ALK60-150	0.4421	0.4051		
CMO-ALK60-200	0.4336	0.3865		
CMO-ALK60-250	0.4025	0.3404	0.0778	0.0885
CMO-AC45-100	0.3952	0.4506		
CMO-AC45-150	0.4988	0.4579		
CMO-AC45-200	0.5118	0.4791		
CMO-AC45-250	0.4656	0.4235	0.0462	0.0556

that alkali treatment has more advantages than acid treatment in terms of improving oxygen activation and the oxidation capacity of surface active oxygen species.

The H<sub>2</sub>-TPR experiment was used to test the low-temperature reduction performance of oxygen species on the catalysts, and the test results are shown in Fig. 8. The CMO and CMO-AC45 have an clearly visible oxygen species reduction peak at 317 °C and 303 °C, respectively. Furthermore, the CMO-ALK60 has two prominent oxygen species reduction peaks at 245 °C and 293 °C, respectively. The low-temperature reduction performance of oxygen species on the catalyst increases in the following order: CMO < CMO-AC45 < CMO-ALK60, which is in good agreement with the results of O 1s in-situ XPS detection. Both acid and alkali treatment can introduce many oxygen vacancies on the CuMn<sub>2</sub>O<sub>4</sub> spinel surface, and the formation of oxygen vacancies is beneficial to reducing active oxygen species [21,22,42]. The



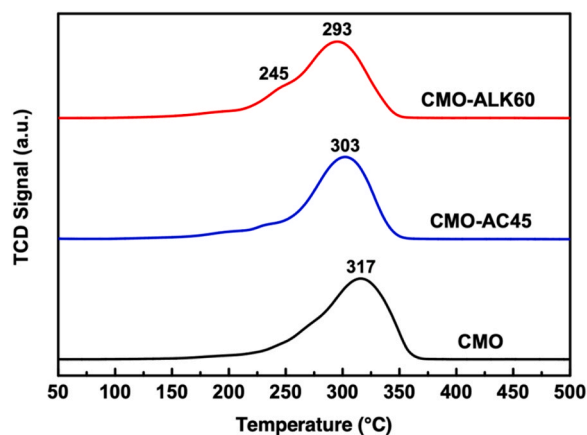


Fig. 8.  $H_2$ -TPR results of the catalysts.

highest amount of oxygen vacancies on the CMO-ALK60 surface results in the highest low-temperature reduction performance.

### 3.4. Reaction mechanism

For observing whether acid and alkali treatment could change toluene activation or oxidation mechanism, the in-situ DRIFTS experiments were performed to detect the intermediates of toluene adsorption and oxidation on CMO, CMO-AC45, and CMO-ALK60. Fig. 9a shows the adsorption of toluene on CMO at 30 °C. The peaks at 1535, 1500, and 1450  $cm^{-1}$  are attributed to the typical aromatic ring structure [45,46]. Additionally, the peaks at 3470 and 3326  $cm^{-1}$  belong to the -OH stretching vibration of adsorbed water, and the peak at 3028  $cm^{-1}$  is ascribed to the -CH<sub>3</sub> stretching vibration [47–49]. The stretching vibration peaks of -CH<sub>2</sub>- are at 2926 and 2871  $cm^{-1}$  [50,51]. The peaks at 1248, 1180, and 1080  $cm^{-1}$  are assigned to C-O stretching vibration of benzyl alcohol, and the peaks at 1746  $cm^{-1}$  and 1670  $cm^{-1}$  belong to benzaldehyde [46,52–54]. In addition, the asymmetric stretching vibration peaks of -COO- appear at 1650 and 1600  $cm^{-1}$ , and the peak at 1390  $cm^{-1}$  is attributed to the symmetric stretching vibration of -COO-, which is ascribed to the benzoate species [46,54,55]. The phenolate (1210 and 1030  $cm^{-1}$ ) and maleic-anhydride (1868 and 1799  $cm^{-1}$ ) were detected, and the shorter-chain olefin or alcohol-containing C=C (940 and 910  $cm^{-1}$ ) were observed [45,50,55–57]. Furthermore, the peaks at 2333 and 2300  $cm^{-1}$  belong to CO<sub>2</sub>, and the peak at 1963  $cm^{-1}$  is attributed to bridge-adsorbed CO [50,55–58]. The adsorption of toluene on CMO-AC45 and CMO-ALK60 at 30 °C are presented in Fig. 9c and e, respectively. The results show that the positions of all peaks on each catalyst are almost the same, which indicates that the toluene activation on each catalyst is almost the same (Fig. 9a, c, and e). However, the highest peak intensity over CMO-AC45 confirms that CMO-AC45 has the strongest adsorption capacity for toluene and intermediates. The CMO and CMO-ALK60 have almost the same adsorption capacity for toluene and intermediates. Fig. 9b, d, and f present the oxidation process of toluene on CMO, CMO-AC45, and CMO-ALK60, respectively. The results show that the intermediates in the toluene oxidation process on each catalyst are the same, proving that the toluene oxidation mechanism is not changed by acid or alkali treatment. Similarly, CMO-AC45 has the most robust adsorption capacity for intermediates, and CMO and CMO-ALK60 have almost the same adsorption capacity for intermediates, which is consistent with the results of the toluene adsorption experiments. In the toluene oxidation process, adsorbed water's peak strength decreased significantly, which was caused by water desorption at high temperatures. Moreover, the toluene oxidation process products include benzyl alcohol, benzoic acid, phenol, maleic-anhydride, shorter-chain olefin, or alcohol-containing C=C, CO, and CO<sub>2</sub>. Different from the toluene adsorption experiment, there is no

benzaldehyde peak in the heating oxidation process, which indicates that the oxidation rate of benzaldehyde to benzoic acid is high-speed. Research has reported that benzoate could not form without O<sub>ads</sub> resulting from oxygen vacancies, and thus the oxygen vacancy is critical for VOCs catalytic combustion [45]. In addition, CMO-ALK60 has the lowest peak intensity of intermediates and the highest peak intensity of final product CO<sub>2</sub>, demonstrating that toluene and its intermediates have the fastest oxidation rate on CMO-ALK60. The oxygen vacancy amount of CMO-ALK60 is the largest, and a large number of oxygen vacancies can provide sufficient active oxygen species for toluene catalytic combustion, thus accelerating the oxidation rate of toluene and intermediates. The catalytic combustion mechanism of toluene is shown in Scheme 1.

### 3.5. Stability evaluation of the catalyst

The high-performance catalytic combustion catalyst not only should have high catalytic activity, but also should have excellent catalytic stability. To further investigate the catalytic stability of CMO-AC45 and CMO-ALK60, a 50-hour continuous catalytic combustion of toluene experiment and the water resistance performance test were conducted, and the results are shown in Fig. 10. The results indicate that the catalytic activity of CMO-AC45 decreases gradually with the increase in reaction time, and finally, deactivation occurs. The catalytic activity of CMO-ALK60 was almost unchanged in the continuous reaction process, indicating that CMO-ALK60 also has high stability. In addition, the water resistance test results showed that water's impact was completely reversible, and the introduction of water neither slowed nor accelerated the deactivation of CMO-AC45. The oxygen vacancy concentrations of the post-reaction catalysts were investigated to reveal the stability of the oxygen vacancy introduced on the catalyst surface. The results are shown in Fig. S7, and the results present that the amount of oxygen vacancy of the pre-reaction CMO-AC45 and CMO-ALK60 is consistent with the number of oxygen vacancy of the post-reaction CMO-AC45 and CMO-ALK60, respectively. The oxygen vacancies introduced on the surface of acid- and alkali-treated catalysts exhibit excellent stability. Moreover, the acidity of catalysts and the amount of carbon deposition on the catalysts were detected to explain the deactivation of CMO-AC45 and the high stability of CMO-ALK60.

The NH<sub>3</sub>-TPD test was used to investigate the acid strength and acid amount of the catalysts, and the results are presented in Fig. 11 and Table 4. The weak acid sites amount of CMO, CMO-AC45, and CMO-ALK60 are 0.0219, 0.0263, and 0.0211 mmol/g, respectively; the moderate strong acid sites are 0.0672, 0.1551, and 0.1931 mmol/g, and the strong acid sites are 0.4736, 0.4764, and 0.3561 mmol/g respectively. And finally, the total acid sites of CMO, CMO-AC45, and CMO-ALK60 are 0.5627, 0.6578, and 0.5703 mmol/g, respectively. Acid treatment could increase the acidity of the catalyst, and the total acid sites were increased by 16.9%. The acid sites can adsorb VOCs, which explains why CMO-AC45 has the strongest adsorption capacity for toluene and its oxidation intermediates [25]. Alkali treatment could increase the number of moderate strong acid sites and reduce the number of strong acid sites. Moreover, the weak and total acid sites of CMO-ALK60 are almost the same as those of CMO. The similar total acid sites of CMO and CMO-ALK60 make them have almost the same adsorption capacity for toluene and its oxidation intermediates. It has been reported that toluene is challenging to oxidize on strong acid sites due to excessive adsorption strength. The toluene is easily converted to polycyclic aromatic hydrocarbons on strong acid sites, resulting in catalyst carbon deposition deactivation [58]. The strong acid sites amount of CMO-ALK60 is 25.3% less than that of CMO-AC45, which makes CMO-ALK60 less prone to carbon deposition on the catalyst surface than CMO-AC45 during 50-hour continuous toluene catalytic combustion.

The results of catalyst carbon deposition are shown in Table S1, and the results indicate that a large amount of carbon species deposited on



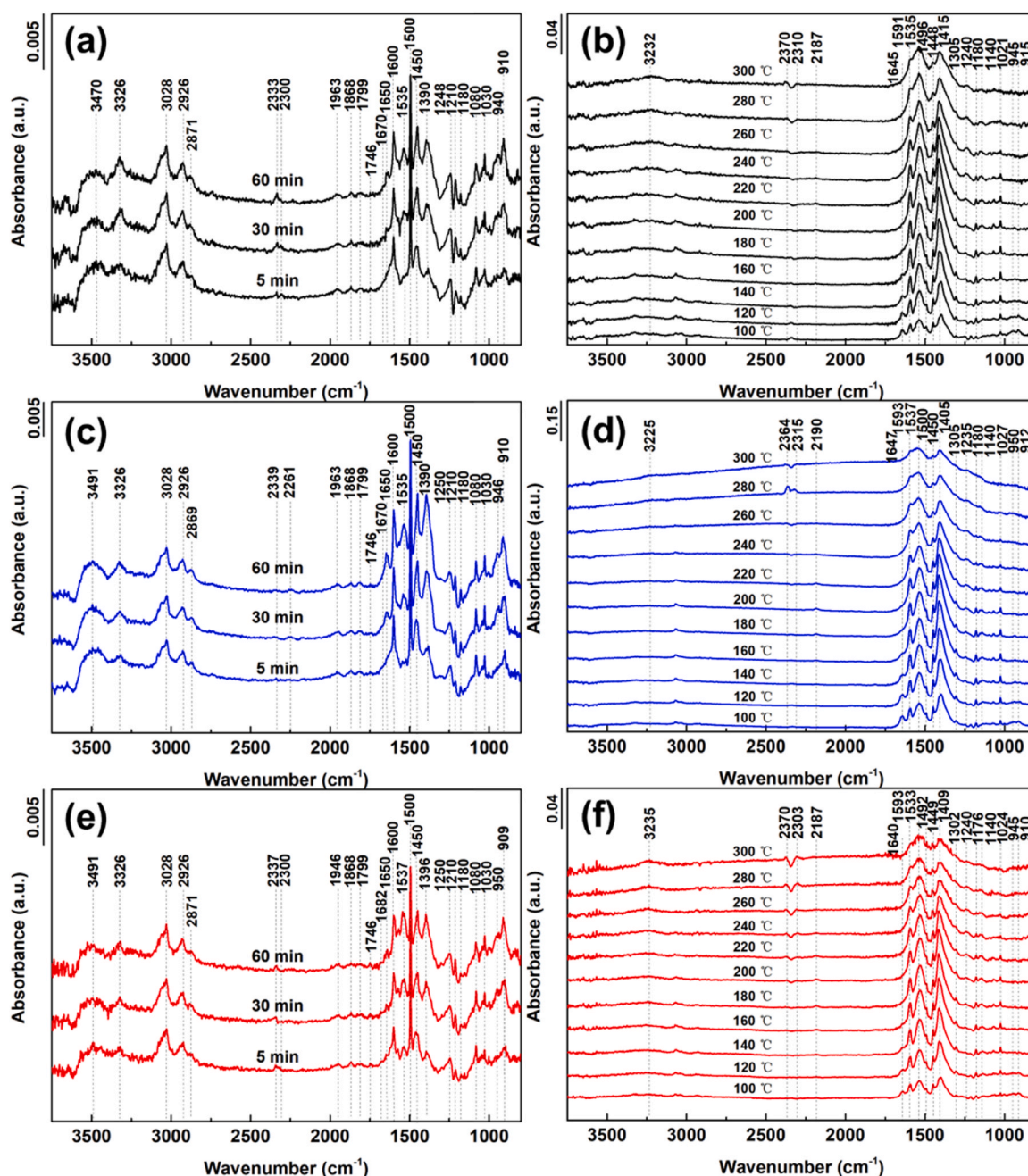


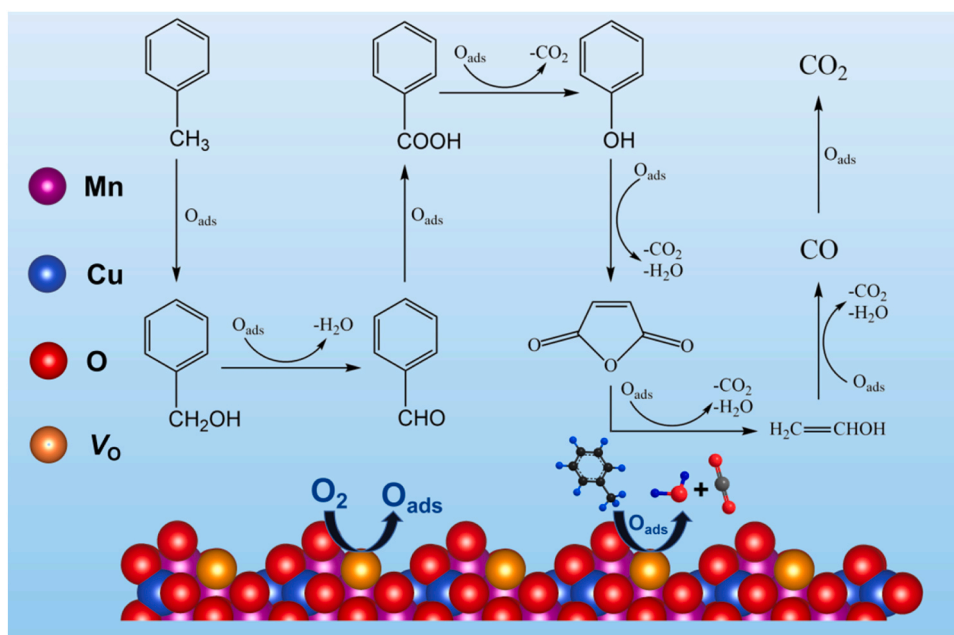
Fig. 9. In situ DRIFT results for (a, c, e) toluene adsorption and (b, d, f) toluene oxidation: (a, b) CMO, (c, d) CMO-AC45, and (e, f) CMO-ALK60.

CMO-AC45 after the 50 h continuous catalytic combustion of toluene. In contrast, the amount of carbon deposition on CMO-ALK60 is much smaller. It has been reported that toluene is challenging to oxidize on strong acid sites due to excessive adsorption strength. The toluene is easily converted to polycyclic aromatic hydrocarbons on strong acid sites, resulting in catalyst carbon deposition deactivation [59]. The strong acid sites amount of CMO-ALK60 is 25.3% less than that of CMO-AC45, which makes CMO-ALK60 less prone to carbon deposition. The TEM images of post-reaction CMO-AC45 and post-reaction CMO-ALK60 (50-hour toluene combustion reaction) are shown in Fig. S8. The results indicate that the pre-reaction CMO-AC45 has a cotton-like structure, and the post-reaction CMO-AC45 no longer exhibits a cotton-like structure due to a large amount of carbon deposition. In contrast, the post-reaction CMO-ALK60 has a small amount of carbon deposition on its surface, which makes the microstructure of post-reaction CMO-ALK60 basically the same as the pre-reaction

CMO-ALK60. Therefore, the alkali-treated catalyst has excellent stability.

#### 4. Conclusion

In summary, lots of oxygen vacancies were precisely introduced on the surface of copper-manganese spinel through acid treatment and alkali treatment, significantly enhancing the catalytic activity of copper-manganese spinel for toluene combustion. The introduction of numerous oxygen vacancies makes it easier for CMO-AC45 and CMO-ALK60 to adsorb and activate oxygen. The activated oxygen on the two catalysts is more likely to participate in the oxidation reaction. The active oxygen species' high content and oxidizing property on CMO-AC45 and CMO-ALK60 accelerate the oxidation rate of toluene. The CMO-ALK60, with more oxygen vacancies, has the highest catalytic combustion activity and stability of toluene. Alkali treatment only



Scheme 1. Reaction mechanism of toluene combustion on the catalysts.

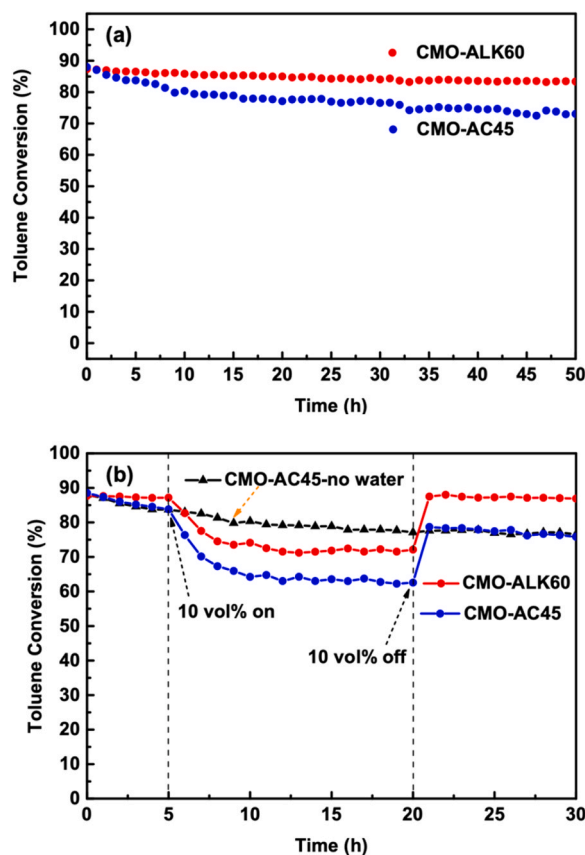


Fig. 10. Catalytic stability test for the catalysts. (a) 50-h continuous catalytic combustion test of toluene, (b) water resistance performance test.

dissolved the Cu species on the surface of copper-manganese spinel, resulting in the formation of the  $\text{Mn}_2\text{O}_3/\text{CuMn}_2\text{O}_4$  composite structure, which preserved the number of oxygen vacancies to the maximum extent. In addition, alkali treatment could adjust the acidity of the catalyst to a more appropriate level, which improved the carbon-

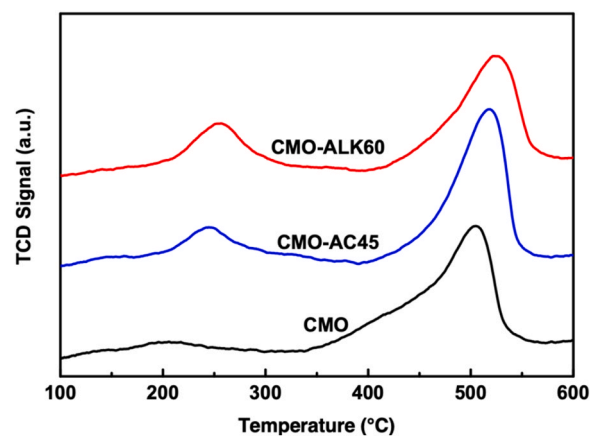
Fig. 11.  $\text{NH}_3$ -TPD results of the catalysts.

Table 4

Surface acid sites of the catalysts ( $\text{NH}_3$ -TPD).

Catalyst	Weak acid sites (mmol/g)	Moderate strong acid sites (mmol/g)	Strong acid sites (mmol/g)	Total acid sites (mmol/g)
CMO	0.0219	0.0672	0.4736	0.5627
CMO-AC45	0.0263	0.1551	0.4764	0.6578
CMO-ALK60	0.0211	0.1931	0.3561	0.5703

deposition resistance of the CMO-ALK60. The appropriate catalyst acidity make CMO-ALK60 possess excellent catalytic stability. This work provides a new path to improve the catalytic combustion activity of copper-manganese spinel and also supplies a low-cost and high-efficiency method for the surface oxygen vacancy engineering development of transition metal oxides, which may have huge potential in other fields.

## CRediT authorship contribution statement

Yu Yang conceived the project and performed most experiments. Junhua Li, Wenzhe Si, Yue Peng and Jianjun Chen supervised and directed the research and manuscript. Yu Wang and Deli Chen conducted data analysis and contributed to manuscript embellishment. Zhenbang Tian and Jing Wang performed the experiments during the process of revising the manuscript. All authors have approved the final version of the manuscript.

## Declaration of Competing Interest

The authors declare no competing financial interest.

## Data Availability

Data will be made available on request.

## Acknowledgement

The authors acknowledge the financial support provided by the National Natural Science Foundation of China (21936005, and 22276105), Beijing Natural Science Foundation (8222054).

## Appendix A. Supporting information

Supplementary data associated with this article can be found in the online version at doi:10.1016/j.apcatb.2023.123142.

## References

- [1] K.R. Bilsback, J. Dahlke, K.M. Fedak, N. Good, A. Hecobian, P. Herckes, C. L'Orange, J. Mehaffy, A. Sullivan, J. Tryner, L. Van Zyl, E.S. Walker, Y. Zhou, J. R. Pierce, A. Wilson, J.L. Peel, J. Volckens, A laboratory assessment of 120 air pollutant emissions from biomass and fossil fuel cookstoves, *Environ. Sci. Technol.* 53 (2019) 7114–7125.
- [2] J.H. Park, A.H. Goldstein, J. Timkovsky, S. Fares, R. Weber, J. Karlik, R. Holzinger, Active atmosphere-ecosystem exchange of the vast majority of detected volatile organic compounds, *Science* 341 (2013) 643–647.
- [3] X. Chen, Q. Luo, D. Wang, J. Gao, Z. Wei, Z. Wang, H. Zhou, A. Mazumder, Simultaneous assessments of occurrence, ecological, human health, and organoleptic hazards for 77 VOCs in typical drinking water sources from 5 major river basins, China, *Environ. Pollut.* 266 (2015) 64–72.
- [4] A. Russell, J. Milford, M.S. Bergin, S. McBride, L. McNair, Y. Yang, W.R. Stockwell, B. Croes, Urban ozone control and atmospheric reactivity of organic gases, *Science* 269 (1995) 491–495.
- [5] D. Han, S. Gao, Q. Fu, J. Cheng, X. Chen, H. Xu, S. Liang, Y. Zhou, Y. Ma, Do volatile organic compounds (VOCs) emitted from petrochemical industries affect regional PM<sub>2.5</sub>? *Atmos. Res.* 209 (2018) 123–130.
- [6] Y. Guo, M. Wen, G. Li, T. An, Recent advances in VOC elimination by catalytic oxidation technology onto various nanoparticles catalysts: a critical review, *Appl. Catal. B Environ.* 281 (2021), 119447.
- [7] L. Ma, C.Y. Seo, X. Chen, J. Li, J.W. Schwank, Sodium-promoted Ag/CeO<sub>2</sub> nanospheres for catalytic oxidation of formaldehyde, *Chem. Eng. J.* 350 (2018) 419–428.
- [8] K. Zhang, H. Ding, W. Pan, X. Mu, K. Qiu, J. Ma, Y. Zhao, J. Song, Z. Zhang, Research progress of a composite metal oxide catalyst for VOC degradation, *Environ. Sci. Technol.* 56 (2022) 9220–9236.
- [9] C. He, J. Cheng, X. Zhang, M. Douthwaite, S. Pattison, Z. Hao, Recent advances in the catalytic oxidation of volatile organic compounds: a review based on pollutant sorts and sources, *Chem. Rev.* 119 (2019) 4471–4568.
- [10] Y. Yang, G. Wang, S. Ge, H. Yang, M. Liu, M. Liu, Study on anti-sulfur dioxide poisoning of palladium-based catalyst for toluene catalytic combustion, *Int. J. Hydrog. Energy* 46 (2021) 6329–6340.
- [11] R.M. Bullock, J.G. Chen, L. Gagliardi, P.J. Chirik, O.K. Farha, C.H. Hendon, C. W. Jones, J.A. Keith, J. Klosin, S.D. Minter, R.H. Morris, A.T. Radosevich, T. B. Rauchfuss, N.A. Strotman, A. Vojvodic, T.R. Ward, J.Y. Yang, Y. Surendranath, Using nature's blueprint to expand catalysis with earth-abundant metals, *Science* 369 (2020).
- [12] Z. Ye, J.M. Giraudon, N. Nuns, P. Simon, N. De Geyter, R. Morent, J.F. Lamonier, Influence of the preparation method on the activity of copper-manganese oxides for toluene total oxidation, *Appl. Catal. B Environ.* 223 (2018) 154–166.
- [13] T. Biemelt, K. Wegner, J. Teichert, M.R. Lohe, J. Martin, J. Grothe, S. Kaskel, Hopcalite nanoparticle catalysts with high water vapour stability for catalytic oxidation of carbon monoxide, *Appl. Catal. B Environ.* 184 (2016) 208–215.
- [14] Y. Yang, J. Liu, F. Liu, Z. Wang, J. Ding, H. Huang, Reaction mechanism for NH<sub>3</sub>-SCR of NO<sub>x</sub> over CuMn<sub>2</sub>O<sub>4</sub> catalyst, *Chem. Eng. J.* 361 (2019) 578–587.
- [15] Z. Wang, J. Liu, Y. Yang, Y. Yu, X. Yan, Z. Zhang, AMn<sub>2</sub>O<sub>4</sub> (A=Cu, Ni and Zn) sorbents coupling high adsorption and regeneration performance for elemental mercury removal from syngas, *J. Hazard. Mater.* 388 (2020), 121738.
- [16] Y. Wang, D. Yang, S. Li, L. Zhang, G. Zheng, L. Guo, Layered copper manganese oxide for the efficient catalytic CO and VOCs oxidation, *Chem. Eng. J.* 357 (2019) 258–268.
- [17] J. Ding, Y. Yang, J. Liu, L. Zhao, Y. Yu, Mechanistic study on the role of oxygen vacancy for methylene chloride oxidation over La-Mn perovskite, *Appl. Surf. Sci.* 559 (2021), 149979.
- [18] M.D. Farahani, M. Wolf, P.O. Mkhwanazi, T. Claeys, M. Friedrich, H. B. Operando experimental evidence on the central role of oxygen vacancies during methane combustion, *J. Catal.* 390 (2020) 184–195.
- [19] D. Ji, L. Fan, L. Tao, Y. Sun, M. Li, G. Yang, T.Q. Tran, S. Ramakrishna, S. Guo, The Kirkendall effect for engineering oxygen vacancy of hollow Co<sub>3</sub>O<sub>4</sub> nanoparticles toward high-performance portable zinc-air batteries, *Angew. Chem.* 58 (2019) 13840–13844.
- [20] S. Zhao, C. Tan, C.-T. He, P. An, F. Xie, S. Jiang, Y. Zhu, K.-H. Wu, B. Zhang, H. Li, J. Zhang, Y. Chen, S. Liu, J. Dong, Z. Tang, Structural transformation of highly active metal-organic framework electrocatalysts during the oxygen evolution reaction, *Nat. Energy* 5 (2020) 881–890.
- [21] J. Yang, S. Hu, Y. Fang, S. Hoang, L. Li, W. Yang, Z. Liang, J. Wu, J. Hu, W. Xiao, C. Pan, Z. Luo, J. Ding, L. Zhang, Y. Guo, Oxygen vacancy promoted O<sub>2</sub> activation over perovskite oxide for low-temperature CO oxidation, *ACS Catal.* 9 (2019) 9751–9763.
- [22] Y. Zheng, K. Fu, Z. Yu, Y. Su, R. Han, Q. Liu, Oxygen vacancies in a catalyst for VOCs oxidation: synthesis, characterization, and catalytic effects, *J. Mater. Chem. A* 10 (2022) 14171–14186.
- [23] X. Lin, S. Li, H. He, Z. Wu, J. Wu, L. Chen, D. Ye, M. Fu, Evolution of oxygen vacancies in MnO<sub>x</sub>-CeO<sub>2</sub> mixed oxides for soot oxidation, *Appl. Catal. B Environ.* 223 (2018) 91–102.
- [24] Y. Wang, L. Guo, M. Chen, C. Shi, CoMn<sub>2</sub>O<sub>7</sub> nanosheets with molecular-scale homogeneity: an excellent catalyst for toluene combustion, *Catal. Sci. Technol.* 8 (2018) 459–471.
- [25] Y. Yang, G. Wang, P. Zheng, F. Dang, J. Han, Carbon deposits during catalytic combustion of toluene on Pd-Pt-based catalysts, *Catal. Sci. Technol.* 10 (2020) 2452–2461.
- [26] S. Schauermaann, C. Schröder, M.C. Schmidt, P.A. Haugg, A.K. Baumann, J. Smyczek, Understanding ligand-directed heterogeneous catalysis: when the dynamically changing nature of the ligand layer controls the hydrogenation selectivity, *Angew. Chem. Int. Ed.* 60 (2021) 16349–16354.
- [27] W. Guo, L. Cui, H. Xu, C. Gong, Selective dissolution of A-site cations of La<sub>0.8</sub>Pr<sub>0.4</sub>Co<sub>0.8</sub>Fe<sub>0.2</sub>O<sub>3</sub> perovskite catalysts to enhance the oxygen evolution reaction, *Appl. Surf. Sci.* 529 (2020), 147165.
- [28] B. Li, Q. Yang, Y. Peng, J. Chen, L. Deng, D. Wang, X. Hong, J. Li, Enhanced low-temperature activity of LaMnO<sub>3</sub> for toluene oxidation: the effect of treatment with an acidic KMnO<sub>4</sub>, *Chem. Eng. J.* 366 (2019) 92–99.
- [29] Q. Yang, D. Wang, C. Wang, X. Li, K. Li, Y. Peng, J. Li, Facile surface improvement method for LaCoO<sub>3</sub> for toluene oxidation, *Catal. Sci. Technol.* 8 (2018) 3166–3173.
- [30] J. Yang, S. Hu, Y. Fang, S. Hoang, L. Li, W. Yang, Z. Liang, J. Wu, J. Hu, W. Xiao, C. Pan, Z. Luo, J. Ding, L. Zhang, Y. Guo, Oxygen vacancy promoted O<sub>2</sub> activation over perovskite oxide for low-temperature CO oxidation, *ACS Catal.* 9 (2019) 9751–9763.
- [31] Y. Yang, W. Si, Y. Peng, Y. Wang, H. Liu, Z. Su, J. Li, Defect engineering on CuMn<sub>2</sub>O<sub>4</sub> spinel surface: a new path to high-performance oxidation catalysts, *Environ. Sci. Technol.* 56 (2022) 16249–16258.
- [32] P. Wang, J. Wang, X. An, J. Shi, W. Shangguang, X. Hao, G. Xu, B. Tang, A. Abudula, G. Guan, Generation of abundant defects in Mn-Co mixed oxides by a facile agar-gel method for highly efficient catalysis of total toluene oxidation, *Appl. Catal. B Environ.* 282 (2021), 119560.
- [33] Z. Li, D. Liu, Y. Cai, Y. Wang, J. Teng, Adsorption pore structure and its fractal characteristics of coals by N<sub>2</sub> adsorption/desorption and FESEM image analyses, *Fuel* 257 (2019), 116031.
- [34] W.Z. Si, Y. Wang, Y. Peng, J.H. Li, Selective dissolution of A-site cations in ABO<sub>3</sub> perovskites: a new path to high-performance, *Catal., Angew. Chem. Int. Ed.* 54 (2015) 7954–7957.
- [35] Q. Yang, X. Wang, X. Wang, Q. Li, L. Li, W. Yang, X. Chu, H. Liu, J. Men, Y. Peng, Y. Ma, J. Li, Surface reconstruction of a mullite-type catalyst via selective dissolution for NO oxidation, *ACS Catal.* 11 (2021) 14507–14520.
- [36] T.Y. Ma, S. Dai, M. Jaroniec, S.Z. Qiao, Graphitic carbon nitride nanosheet-carbon nanotube three-dimensional porous composites as high-performance oxygen evolution electrocatalysts, *Angew. Chem.* 53 (2014) 7281–7285.
- [37] Z. Cheng, Z. Chen, J. Li, S. Zuo, P. Yang, Mesoporous silica-pillared clays supported nanosized Co<sub>3</sub>O<sub>4</sub>-CeO<sub>2</sub> for catalytic combustion of toluene, *Appl. Surf. Sci.* 459 (2018) 32–39.
- [38] S. Lee, G. Yoon, M. Jeong, M.J. Lee, K. Kang, J. Cho, Hierarchical surface atomic structure of a manganese-based spinel cathode for lithium-ion, *Batter., Angew. Chem. Int. Ed.* 54 (2015) 1153–1158.
- [39] Z. Ye, J.-M. Giraudon, N. Nuns, G. Abdallah, A. Addad, R. Morent, N. De Geyter, J.-F. Lamonier, Preferential dissolution of copper from Cu-Mn oxides in strong acid medium: effect of the starting binary oxide to get new efficient copper doped MnO<sub>2</sub> catalysts in toluene oxidation, *Appl. Surf. Sci.* 537 (2021), 147993.
- [40] Y. Xu, Z. Qu, Y. Ren, C. Dong, Enhancement of toluene oxidation performance over Cu-Mn composite oxides by regulating oxygen vacancy, *Appl. Surf. Sci.* 560 (2021), 149983.



- [41] Y. He, L. Zhang, H.-W. Xiong, X. Kang, Evolution of lattice defects in nickel ferrite spinel: oxygen vacancy and cation substitution, *J. Alloy Compd.* 917 (2022), 165494.
- [42] Z. Su, W. Yang, C. Wang, S. Xiong, X. Cao, Y. Peng, W. Si, Y. Weng, M. Xue, J. Li, Roles of oxygen vacancies in the bulk and surface of CeO<sub>2</sub> for toluene catalytic combustion, *Environ. Sci. Technol.* 54 (2020) 12684–12692.
- [43] X. Zhang, H. Zhao, Z. Song, W. Liu, J. Zhao, Z. a Ma, M. Zhao, Y. Xing, Insight into the effect of oxygen species and Mn chemical valence over MnO on the catalytic oxidation of toluene, *Appl. Surf. Sci.* 493 (2019) 9–17.
- [44] R. Huang, L. Luo, W. Hu, Z. Tang, X. Ji, L. Chen, Z. Yu, Y. Zhang, D. Zhang, P. Xiao, Insight into the pH effect on the oxygen species and Mn chemical valence of Co-Mn catalysts for total toluene oxidation, *Catal. Sci. Technol.* 12 (2022) 4157–4168.
- [45] M.D. Hernández-Alonso, I. Tejedor-Tejedor, J.M. Coronado, M.A. Anderson, Operando FTIR study of the photocatalytic oxidation of methylcyclohexane and toluene in air over TiO<sub>2</sub>-ZrO<sub>2</sub> thin films: Influence of the aromaticity of the target molecule on deactivation, *Appl. Catal. B Environ.* 101 (2011) 283–293.
- [46] H. Sun, Z. Liu, S. Chen, X. Quan, The role of lattice oxygen on the activity and selectivity of the OMS-2 catalyst for the total oxidation of toluene, *Chem. Eng. J.* 270 (2015) 58–65.
- [47] S.P. Rong, P.Y. Zhang, Y.J. Yang, L. Zhu, J.L. Wang, F. Liu, MnO<sub>2</sub> framework for instantaneous mineralization of carcinogenic airborne formaldehyde at room temperature, *ACS Catal.* 7 (2017) 1057–1067.
- [48] J. Wang, J. Li, C. Jiang, P. Zhou, P. Zhang, J. Yu, The effect of manganese vacancy in birnessite-type MnO<sub>2</sub> on room-temperature oxidation of formaldehyde in air, *Appl. Catal. B Environ.* 204 (2017) 147–155.
- [49] J.Y. Li, X.A. Dong, G. Zhang, W. Cui, W.L. Cen, Z.B. Wu, S.C. Lee, F. Dong, Probing ring-opening pathways for efficient photocatalytic toluene decomposition, *J. Mater. Chem. A* 7 (2019) 3366–3374.
- [50] C. Zhang, H. He, K.-i Tanaka, Catalytic performance and mechanism of a Pt/TiO<sub>2</sub> catalyst for the oxidation of formaldehyde at room temperature, *Appl. Catal. B Environ.* 65 (2006) 37–43.
- [51] M. Hosseini, T. Barakat, R. Cousin, A. Aboukais, B.L. Su, G. De Weireld, S. Siffert, Catalytic performance of core-shell and alloy Pd-Au nanoparticles for total oxidation of VOC: the effect of metal deposition, *Appl. Catal. B Environ.* 111 112 (2012) 218–224.
- [52] J.J. Li, S.C. Cai, X. Chen, D.X. Yan, J. Chen, H.P. Jia, Engineering rGO nanosheets-adsorption layer supported Pt nanoparticles to enhance photo-thermal catalytic activity under light irradiation, *J. Mater. Chem. A* 7 (2019) 11985–11995.
- [53] V. Augugliaro, H. Kisch, V. Loddo, M.J. López-Muñoz, C. Márquez-Álvarez, G. Palmisano, L. Palmisano, F. Parrino, S. Yurdakal, Photocatalytic oxidation of aromatic alcohols to aldehydes in aqueous suspension of home prepared titanium dioxide, *Appl. Catal. A-Gen.* 349 (2008) 189–197.
- [54] K. Li, J. Chen, B. Bai, S. Zhao, F. Hu, J. Li, Bridging the reaction route of toluene total oxidation and the structure of ordered mesoporous Co<sub>3</sub>O<sub>4</sub>: The roles of surface sodium and adsorbed oxygen, *Catal. Today* 297 (2017) 173–181.
- [55] S.P. Mo, Q. Zhang, Y.H. Sun, M.Y. Zhang, J.Q. Li, Q.M. Ren, M.L. Fu, J.L. Wu, L. M. Chen, D.Q. Ye, Gaseous C.O. and toluene co-oxidation over monolithic core-shell Co<sub>3</sub>O<sub>4</sub>-based hetero-structured catalysts, *J. Mater. Chem. A* 7 (2019) 16197–16210.
- [56] H. Huang, Y. Gu, J. Zhao, X. Wang, Catalytic combustion of chlorobenzene over VO<sub>x</sub>/CeO<sub>2</sub> catalysts, *J. Catal.* 326 (2015) 54–68.
- [57] A.L. Lu, H.L. Sun, N.W. Zhang, L.M. Che, S.Y. Shan, J. Luo, J.B. Zheng, L.F. Yang, D. L. Peng, C.J. Zhong, Surface partial-charge-tuned enhancement of catalytic activity of platinum nanocatalysts for toluene oxidation, *ACS Catal.* 9 (2019) 7431–7442.
- [58] C.Y. Ma, D.H. Wang, W.J. Xue, B.J. Dou, H.L. Wang, Z.P. Hao, Investigation of formaldehyde oxidation over Co<sub>3</sub>O<sub>4</sub>-CeO<sub>2</sub> and Au/Co<sub>3</sub>O<sub>4</sub>-CeO<sub>2</sub> catalysts at room temperature: effective removal and determination of reaction mechanism, *Environ. Sci. Technol.* 45 (2011) 3628–3634.
- [59] M. Guisnet, E. Dege, P. Magnoux, Catalytic oxidation of volatile organic compounds 1. Oxidation of xylene over a 0.2 wt% Pd/HFAU(17) catalyst, *Appl. Catal. B Environ.* 20 (1999) 1–13.